Combustion and Flame xxx (xxxx) xxx

Contents lists available at ScienceDirect

Combustion and Flame

journal homepage: www.sciencedirect.com/journal/combustion-and-flame

Laminar flame speed modification by nanosecond repetitively pulsed discharges, Part II: Experiments

Colin A. Pavan *, Carmen Guerra-Garcia *

Massachusetts Institute of Technology, Department of Aeronautics and Astronautics, 77 Massachusetts Ave, Cambridge, 02141, MA, USA

ARTICLE INFO

Keywords:
Laminar flame speed
1D numerical model
Plasma-assisted combustion (PAC)
Nanosecond Repetitively Pulsed Discharges (NRPD)
Beneficial and adverse effects of plasma
Optimization of plasma actuation strategy
Narrow channel burner
Transparent electrodes

ABSTRACT

This paper systematically evaluates how, and to what extent, nanosecond repetitively pulsed (NRP) discharges modify the laminar flame speed of methane–air mixtures at ambient conditions, using both experiments in a narrow-channel quartz burner and a one-dimensional plasma-combustion model described in an accompanying paper (Part I). By varying the discharge location relative to the flame, four actuation strategies were explored at variable pulse repetition frequency: (i) discharges far ahead of the flame, (ii) pre-treatment of fresh reactants, (iii) direct (insitu) plasma–flame overlap, and (iv) a combination of pre-treatment and insitu interaction. Results show that acoustic waves produced by upstream discharges can reduce flame speed by as much as 30%–40%; while partially overlapping the discharge with the flame significantly accelerates it, with measured enhancements of up to 50% in both model and experiment. Flame speed modification by plasma increased with pulse repetition frequency, so that the envelope of performance enhancement reported here is limited by the highest frequencies tested (8kHz). The model captures these trends by attributing the detrimental effects to pressure-wave disturbances and the beneficial effects to radical-seeding and mild heat addition in, and close to, the reaction zone. These observations may help shed light on previously reported experiments and are here presented in a unified manner by focusing on a fundamental combustion metric (laminar flame speed), to give generality to the results obtained in laminar flames. The results demonstrate how spatio-temporal positioning of the discharge governs whether plasma aids or hinders the flame, ultimately guiding the design of optimal plasma-assisted combustion strategies.

Novelty and Significance Statement

This work provides a systematic evaluation of how nanosecond repetitively pulsed discharges can either accelerate or disrupt premixed methane–air flames, depending on their spatial and temporal overlap with the flame front. This is the first time a comprehensive study on the influence of plasmas on laminar flame speed has been conducted, which allows to compare different strategies. By combining a narrow-channel experimental burner and a one-dimensional plasma-combustion model, the study clarifies the mechanisms of interaction that drive flame-speed modifications. Namely, radical seeding, heat addition, and pressure-wave disturbances. The ability to directly compare different discharge strategies within a common framework helps reconcile a wide range of flame-speed enhancements reported in the literature. These findings offer new insights into plasma–flame coupling and can be used to guide the design of more effective plasma-assisted combustion systems.

1. Introduction

Premixed laminar flames, in which fuel and oxidizer are homogeneously combined prior to combustion, can be characterized by their laminar flame speed: the rate at which the flame front propagates into a quiescent mixture. This fundamental parameter is a key metric for understanding and modeling premixed combustion, serving as a baseline from which more complex turbulent flame behaviors can be interpreted. Although laminar flame speed is traditionally governed by the balance of diffusive transport and chemical kinetics, advances in plasma-assisted combustion (PAC) suggest that non-thermal processes can supplement purely thermal pathways in driving flame propagation.

Much of the work on PAC has focused on ignition enhancement and flame stabilization in high-speed flows, swirl combustors, or bluff-body systems prone to blow-off. In these applications, plasma discharges

* Corresponding authors.
E-mail addresses: cpavan@mit.edu (C.A. Pavan), guerrac@mit.edu (C. Guerra-Garcia).

https://doi.org/10.1016/j.combustflame.2025.114475
Received 8 March 2025; Received in revised form 7 September 2025; Accepted 9 September 2025

have proven effective in shortening ignition delay times (e.g., in shock-tube experiments [1–3]) and expanding lean blow-off limits (e.g., in swirled combustors [4–7]). Several studies have demonstrated that nanosecond repetitively pulsed discharges can introduce radicals, modify low-temperature chemistry, and locally heat the mixture, thus accelerating the onset of ignition in challenging environments. Recent numerical efforts in multi-dimensional configurations [8,9] similarly highlight plasma-driven pathways that enhance or sustain turbulent flames. However, these high-speed or turbulent conditions obscure the direct impact of plasma on the fundamental flame speed itself, combining kinetic effects with complex flow patterns and residence time constraints.

By contrast, there have been only a few attempts to isolate plasma effects on laminar premixed flames where flow complexities are minimized. For instance, Evans et al. [10] observed an upstream shift of a lean laminar flame under a nanosecond pulsed discharge, attributing the effect to enhanced radical production. Elkholy et al. [11] similarly recorded a significant increase in laminar flame speed when a dielectric barrier discharge was applied, in this case attributing most of the measured gain to gas heating by the plasma. These examples illustrate that although PAC can indeed alter laminar flame behavior, the underlying mechanisms remain insufficiently understood. Additionally, it is unclear what is the envelope of performance enhancement when actuating with plasma, as reported flame speed increases range between 2–3% [12] and 100% [11].

There is a knowledge gap concerning how, and to what extent, plasma discharges can modify laminar flame speeds. A deeper understanding of these interactions requires a systematic evaluation of plasma's direct impact on the flame, including a parametric exploration of electrical inputs (e.g., pulse repetition frequency) and actuation strategies (e.g., positioning of the discharge relative to the flame front). This paper aims to fill that gap by leveraging the numerical model introduced in Part I and corroborating its predictions with an accompanying experiment to elucidate the mechanisms governing the influence of plasma on laminar flame speed modification for methane/air premixed flames at ambient conditions.

The paper is divided as follows. Section 2 describes the experimental setup used which mimics the layout of the numerical model in Part I and uses transparent electrodes to visualize flame propagation. The post-processing algorithms to recover flame speed from the imaging study are defined. Section 3 summarizes the test cases for evaluating the influence of plasma on laminar flame speed propagation, and defines both the parameters for the numerical model and the accompanying experiment. Sections 4–7 explore the impact of pulsed nanosecond discharge actuation on the laminar flame for different actuation strategies including discharge pre-treatment of reactants and in-situ plasma deposition. Discussion and conclusions are summarized in sections 8 and 9, respectively.

This work explores an inherently transient process. The included figures have been constructed to convey the transient evolution of the system as best as possible, but additional information on the time evolution can still be obtained from viewing videos of the experiment and simulation results. For each strategy, in both simulation and experiment, a video has been included in the supplementary materials. The reader is encouraged to view these materials as part of the work.

2. Experimental methods

2.1. Experimental setup

The experimental setup is described in the authors previous work [13–15] and is summarized here for completeness. It consists of a transparent quartz burner, with rectangular cross section, and with a premixed flame propagating counter the flow of reactant gases. The burner is tapered, with premixed methane–air entering the narrow end and being ignited at the wide end. The burner varies in height from 4.2 mm to 1 mm over 20 cm on the wet side (internal surface, in contact with the process gas, Fig. 1(a)), and is 3 cm wide. Thermal quenching of the flame for a stoichiometric methane/air mixture happens at around 2.3 mm of height in this experimental setup. The tapered geometry was originally designed for experiments on quenching distance modification by plasma, but it proved useful for flame speed measurements given the clear optical access [14]. The height variation is very gradual, so that over short distances the two sides of the channel can be considered parallel: e.g., over 1 cm, the height varies by less than 0.2 mm. The transparent walls, of 2 mm thickness, allow optical access and having the flame propagate counter to the flow of reactant gases slows propagation in the laboratory reference frame, facilitating high-speed imaging.

A transient electric field is applied orthogonal to the flow of gas. High voltage is applied using a nanosecond pulse generator (Transient Plasma Systems SSPG-20X-HP1) to generate Nanosecond Repetitively Pulsed Discharges (NRPD). The high voltage electrode is made of a 1.1 mm thick glass plane coated in indium tin oxide (ITO) which is affixed to the quartz burner on the dry side of the test section. The electrode is 2.5 cm wide and 3.5 cm long in the streamwise direction, and is placed centered to yield a 3.4 mm discharge-gap, on average. The ITO layer has a nominal thickness of 185 nm and a nominal resistance of 10–15 Ω in^{-2}. The ITO has a slight yellow tinge in appearance and provides 70%–90% transmittance to visible light [16]. The ground electrode is an aluminum plate that also acts as a support for the test section.

The system is viewed by a high speed camera (Edgertronic SC2+) and electrical measurements are taken using a high voltage probe (Lecroy PPE 20 kV) and a Rogowski-coil style current monitor (Pearson model 2877) placed on the current return side of the circuit, using the methods outlined in [17]. The primary metric used for this work, to quantify the impact of plasma on flame, is measurement of the flame velocity, which is done using flame tracking via the high speed video. This is described in more detail in sections 2.2 and 2.3.

The experimental setup is shown schematically in Fig. 1(a). The high speed camera is positioned overhead to view the system through the ITO electrode, with the line-of-sight being parallel to the main electric field direction. An example image as seen by this camera is shown in Fig. 1(b) along with the coordinate system datum that is used for all analysis. The gas flows from right to left in this image, and the channel height is greatest at the left edge. The black object at the far left of the domain is the 3D-printed adaptor connecting the test section to the spark plug ignition cell. The flame travels from left to right, counter the flow of gas as shown in Fig. 1(a). In this work, the direction along the flow (horizontal in Fig. 1(b)) will be referred to as the *streamwise*, or x direction, and the direction across the flow (vertical in Fig. 1(b)) will be referred to as the *spanwise* or y direction. The discharge is applied using an electric field oriented along the z axis.

The control parameters in any set of tests are the electrical parameters for pulse repetition frequency (PRF), voltage (V), number of pulses (N_p), and the actuation strategy quantified by the timing of the onset of the pulses relative to the flame front location; as well as the gas state parameters measured as the equivalence ratio (ϕ) and the total flow rate (Q).

2.2. Flame front identification

The primary parameter of interest is the flame speed, which is measured in the laboratory reference frame using high speed videography with the camera line of sight (LOS) parallel to the dominant electric field direction. Several sample images of the flame, for a given test as a function of time, are shown in Fig. 2. A two-lobe structure is clearly visible in several of these frames. This is a tulip-flame structure [18] typical of narrow-channel flames.

In order to distinguish the flame front from the discharge, high speed videos were taken at twice the pulse repetition frequency of

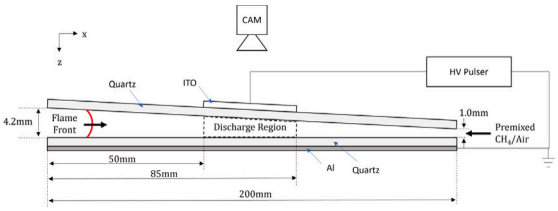

(a) Schematic of the configuration used for the experiments in this work.

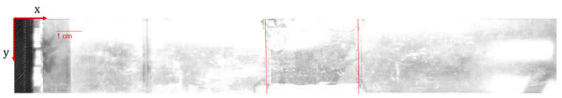

(b) Image of test section as seen by the high speed camera. Electrode boundaries, 35mm apart, are marked by the two red vertical lines.

Fig. 1. Images of the experimental setup and burner test section.

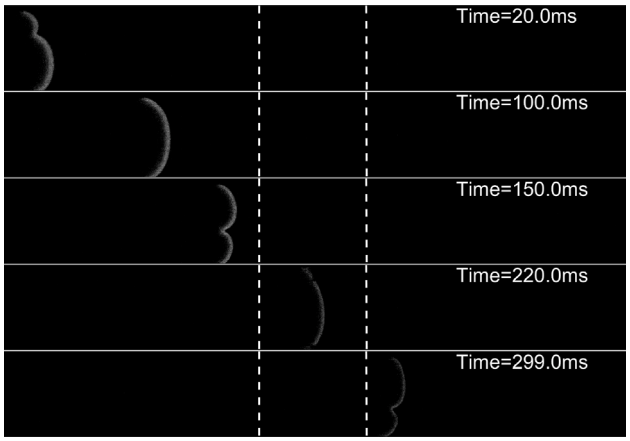

Fig. 2. Several images of the flame with no discharge indicating non-planar flame front. Time stamps refer to time since video start. Electrode marked with white dashed lines. Video is taken at 2 kfps with exposure 1/2012s and artificially brightened during post-processing to clearly show flame front.

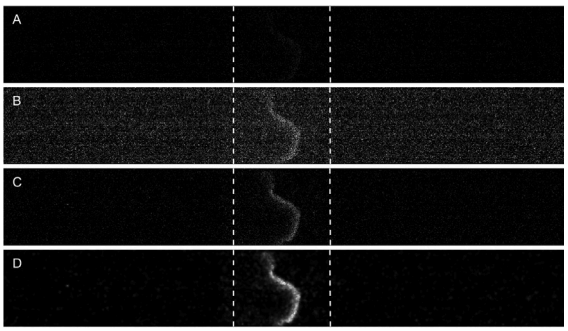

(a) Processing of raw video to identify flame front. Electrode marked by vertical dashed white lines in all images. (A) Raw video frame, taken at 16kfps with 1/16800s exposure. (B) Summation of 8 sequential frames taken between pulses (effective frame rate 1kfps). (C) Mean background removed. (D) Median and guided filters applied, image normalized by maximum intensity pixel.

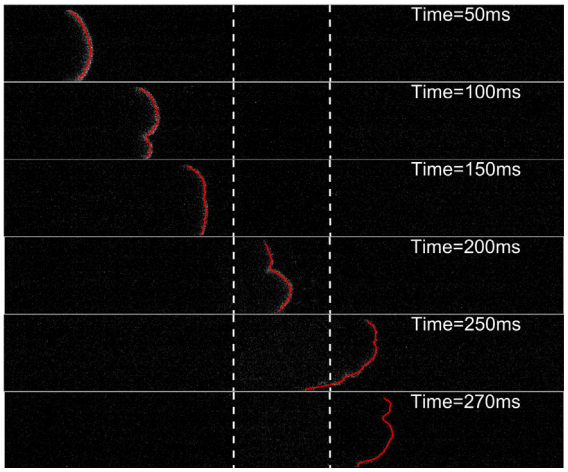

(b) Image of the flame, processed the same as subplot (D) in figure 3a, with the calculated flame front superimposed in red. PRF=8khz, camera frame rate 16kfps, electrode marked by white vertical lines.

Fig. 3. Flame front identification algorithm.

the applied pulsed-nanosecond voltage. The discharge only produced significant light for a short time of hundreds of nanoseconds, so this resulted in alternating frames of coupled discharge-plus-flame and flame-only frames. While the discharge was relatively easy to distinguish, the flame front was much less luminous and significant gain had to be applied to the camera when using high pulse repetition frequencies (PRFs). To identify the flame front in the low light/noisy environment, several steps of video post-processing were applied. First, frames with discharge present (every second frame) were discarded. Then, with the remaining frames, several sequential frames were combined to increase the light; this reduces the effective frame rate but effectively increases the exposure time of the camera. An effective frame rate of 1 kfps was used unless otherwise noted. A typical flame speed is 40 cm/s, so a frame rate of 1 kfps will result in the flame moving 0.4 mm, or about 2.4 pix, per frame, which is much less than the extent of the flame luminosity due to a non-planar flame front in the z-direction. Additional image filtering was then applied to remove the background and salt-and-pepper noise resulting from the high gain that needed to be used. A comparison of the original image with the processed one after each of these steps is shown in Fig. 3(a). After extracting a clear image of the flame front, a curve was fit to obtain the function $x_f(t, y)$ describing the position of the flame front as a function of spanwise position (y) at every point in time (t). Examples of these fitted curves are shown in Fig. 3(b).

2.3. Calculation of flame speed

After obtaining $x_f(t, y)$ using the method outlined in Section 2.2, this must be converted to a flame speed. It is assumed that the flame propagation direction is normal to the flame front; this is true in the reference frame of the flame front and is an acceptable approximation in the laboratory frame provided the oncoming gas velocity is low. For all of the experiments presented with this configuration, the gas flow rate is 400sccm, which gives a mean flow speed of 6.5 cm/s under the electrode. This is a small fraction of the expected flame speed, so the assumption is reasonable. By not accounting for the bulk flow, the flame speed that is calculated will be the laboratory-frame flame speed.

The calculation of flame speed in 2D is derived as follows. $x_f(t, y)$ is a scalar field describing the position of the flame in the streamwise direction at every timestep and spanwise position. Let $\boldsymbol{r}$ be a point on the flame front, defined by

$$\boldsymbol{r}_f(t) = \begin{bmatrix} x_f(t, y) \\ y \end{bmatrix} \tag{1}$$

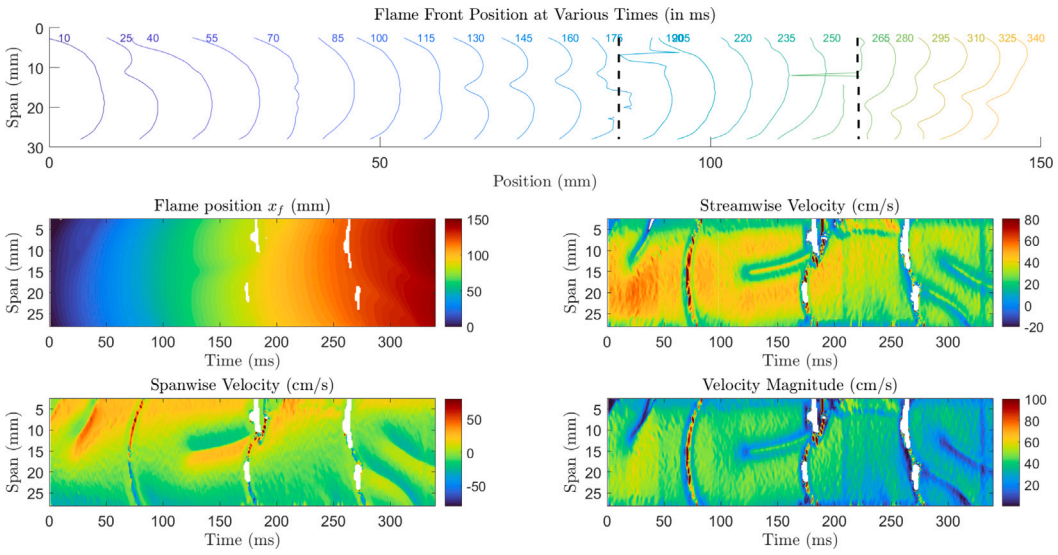

Fig. 4. (Top) flame front position at 15 ms time steps. Dashed black lines indicate electrode position. (Bottom 4 plots) contour plots of flame position and speed as a function of time and spanwise position. Case for no discharge with video at 2 kfps.

The flame velocity is defined as the motion of $\boldsymbol{r}$ with respect to time, which can be calculated by the chain rule as

$$\boldsymbol{v}_f(t) = \frac{d\boldsymbol{r}_f}{dt} = \begin{bmatrix} x_t + x_y y_t \\ y_t \end{bmatrix} \tag{2}$$

where the subscripts t or y indicate the partial derivative, of the flame coordinates x_f and y, with respect to that variable. x_t and x_y can be calculated numerically by taking the partial derivatives of the scalar field $x_f(t, y)$ with respect to its coordinate axes. The unknown is y_t, which can be determined using the assumption that the flame propagation direction is normal to the flame front. To this end, the local reference frame at each point along the frame front needs to be used.

In this local frame, the flame front velocity can be defined as

$$\boldsymbol{v_f} = v_n \hat{\boldsymbol{n}} \tag{3}$$

where v_n is the signed value of the speed in the normal direction, $\hat{\boldsymbol{n}}$. Note that a negative value implies propagation in a direction with negative x component due to the definition of $\hat{\boldsymbol{n}}$. The unit normal to the flame front, with positive x-component, is given by:

$$\hat{\boldsymbol{n}} = \frac{1}{\sqrt{1 + x_y^2}} \begin{bmatrix} 1 \\ -x_y \end{bmatrix} \tag{4}$$

From Eqs. (2), (3), and (4), the unknowns y_t and v_n can be isolated and the flame velocity and its magnitude can then be written as Eqs. (5) and (6) respectively.

$$\boldsymbol{v}_f(t) = \frac{x_t}{1 + x_y^2} \begin{bmatrix} 1 \\ -x_y \end{bmatrix} \tag{5}$$

$$|\boldsymbol{v}_f(t)| = \frac{|x_t|}{\sqrt{1 + x_y^2}} \tag{6}$$

Both of these can be directly calculated from the partial derivatives of $x_f(t, y)$ with respect to the coordinates t and y. To account for bulk flow, Eq. (3) could be modified by adding the bulk flow velocity vector, $\boldsymbol{v}_b$, to the right hand side to get:

$$\boldsymbol{v}_{f,g}(t) = \frac{x_t - v_b}{1 + x_y^2} \begin{bmatrix} 1 \\ -x_y \end{bmatrix} \tag{7}$$

$$|\boldsymbol{v}_{f,g}(t)| = \frac{|x_t - v_b|}{\sqrt{1 + x_y^2}} \tag{8}$$

where $v_b < 0$ is the bulk velocity of the oncoming gas, assumed to be purely in the streamwise direction, and $\boldsymbol{v}_{f,g}$ is the flame speed in the gas reference frame. Unless otherwise noted, the analysis will be performed in the laboratory frame using Eqs. (5) and (6) since there is some uncertainty in the value of v_b due to boundary layers and the diverging channel in this narrow-channel configuration.

2.4. Example of baseline flame (No Discharge)

As an example, the results of a baseline experiment with no discharge are shown in Figs. 4 and 5. The parameters used are those described in Section 3.1, which is the no-discharge case baseline that will be used to compare the different plasma actuation strategies. The no-discharge case allows a lower frame rate to be used for the high-speed video, as well as lower gain, which results in smoother contour plots than will be shown for cases with discharge.

Fig. 4 shows the flame position determined at several points in time plotted in space, the scalar field $x_f(t, y)$, and the components and magnitude of v_f plotted in t-y space. The mixed time–space axes are unavoidable since interpolating and plotting against the x-coordinate is not possible as x is not necessarily monotonically increasing with time. The plots are similar to those often produced for solutions to 1D unsteady PDEs illustrating solution characteristics. The plot of spanwise velocity has been multiplied by −1 so that a positive value of speed indicates the flame front is moving upward (negative y direction), and a negative value means it is moving downward (positive y-direction). Fig. 5(a) shows the same plot as the top graph of Fig. 4 with the local velocity vector of the flame front superimposed.

The velocity contour plots with the t-y axes will be used moving forward as they are the easiest way to show the entire 2D velocity field. These images can be difficult to interpret on first inspection. To aid in this interpretation, Fig. 5(b) shows the mapping from x–y coordinate space to the t-y domain. The feature highlighted by arrow B is a piece of kapton tape on the top of the channel that slightly obstructs the view (see Fig. 1(b)). Markers E and F are the left and right edges of the electrode respectively, also covered in kapton tape to reduce coronas in the surrounding air, which results in a distorted view and the poorly resolved speed measurement. Marker D indicates the attachment point of the high voltage connection. As B, D, E, and F, correspond to obstructions in the camera line-of-sight, the flame velocity information in those locations is not accessible. This displays itself as either white regions in the figures, corresponding to ‘not a number’ (e.g., D, E and F, in Fig. 5(b)) or saturated spurious solutions (B in Fig. 5(b)). Note that these features (B, D, E, and F), can be used as identifying features

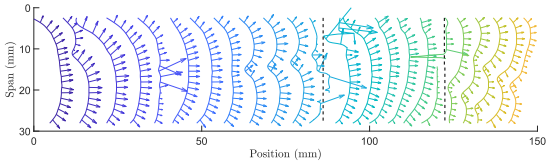

(a) Flame front position and local speed vector. See top graph of figure 4 for time stamps of flame fronts. Arrow lengths scaled so that 1mm on the x/y axis represents 15cm/s.

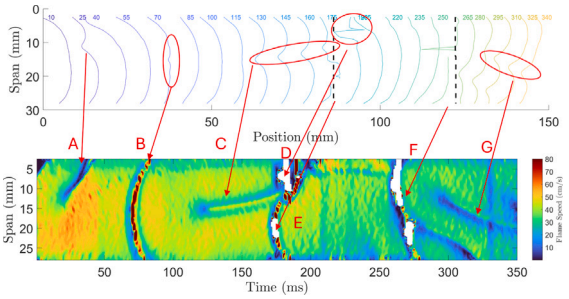

(b) Mapping of flame front shape in x-y plane at various points in time (top graph, label is time in milliseconds) to the space-time velocity contour plot (bottom graph). A, C, G indicate bifurcation points in the flame; B, D, E and F identify obstructions in the camera LOS.

Fig. 5. Flame speed plot interpretation.

for the flame position. In the t-y plot, it is difficult to determine where the flame is located at any given time, but using the feature marked B as reference point it is possible to determine at what time the flame passes the obstruction located at about x = 40 mm. More specifically, at the start of the propagation in the narrow channel, the flame takes a single-lobe shape with the center-point of the flame traveling faster than the locations close to the boundary layers of the channel. Hence, the central point at about 15 mm width, reaches sooner the B-marker (kapton-tape obstruction): marker appears at about 70 ms. The rest of the flame reaches the marker slightly delayed: hence the curved shape displayed on the figure.

Markers A, C and G indicate bifurcation points in the flame which show up as "characteristics" in the t-y plot. The cusps observed at point A, C and G may be tulip-flame structures, which are often observed with flames propagating in tubes [18–20]. These cusps are proposed by Clanet and Searby [18] to be caused by a Rayleigh–Taylor instability [21] although different explanations are favored by other authors [19,20].

3. Parametric exploration of actuation strategies

A set of cases is defined to address how, and to what extent, plasma discharges can modify laminar flame speeds, using the experimental methods of Section 2 and the numerical model of Part I. Premixed methane/air flames, in narrow channels, at ambient pressure and temperature are considered. In particular, a parametric exploration of electrical inputs (e.g., pulse repetition frequency) and actuation strategies (e.g., positioning of the discharge relative to the flame front) is conducted.

Four cases are defined, Fig. 6. Section 4 will investigate a case where the discharge and the flame are separated in space and interact via acoustic waves produced by the discharge (strategy 1). The plasma is produced sufficiently far upstream of the flame that no kinetic or direct-heating effects can contribute to its propagation. The second case is pre-treatment of the reactants by the discharge (strategy 2), discussed in Section 5. In this case, the discharge is applied ahead of the flame but close enough that the produced species and elevated temperatures persist until the flame reaches the electrode. Next, is the insitu discharge (strategy 3), shown in Section 6. For this configuration, the discharge overlaps with the flame front, with the flame starting under the electrode when the plasma is turned on. The final case studied is a combination of the prior two strategies: reactant pre-treatment and insitu discharge (strategy 4). For this configuration, the discharge partially overlaps with the flame front and all effects observed in the previous cases will combine to impact the flame. Specifically, the flame starts slightly ahead of the electrode and passes under it while the nanosecond pulses continue.

This selection of cases covers many of the different configurations other authors have used to study the impact of plasma on laminar flames, and allows to directly compare them. The pre-treatment strategy has typically been explored with burner stabilized flames, for example in Refs. [10,11]. The insitu configuration has been looked at in Ref. [22] for a premixed flame and Ref. [23] for a non-premixed flame. Non-local fluid effects resulting from shocks have been previously observed for ns-sparks in pin-to-pin configurations [24,25] and from low-amplitude pressure waves produced by NRP DBDs in non-reacting flows [26,27].

In all cases, experimental results are presented first and then the numerical model of Part I is used to provide further insights of the mechanisms at play. The parameters used in experiment and model are described in what follows.

3.1. Experiment operating conditions

For all experimental cases, the gas conditions are set constant. The flow is set at 360 sccm of air and 40 sccm of methane. This gives an equivalence ratio of 1.06. Flame power is approximately 125 W.

The electrodes are left fixed for all experiments as described in Section 2, yielding a discharge volume of 3.06 cm^3. The voltage amplitude was set fixed for all cases to give a peak of 22.5 kV (prior to full electrode plasma coverage). This configuration deposits 1–2 mJ per pulse after an initial transient and depending on flame location, corresponding to an energy density of 330–660 $\mu J/cm^3$. This energy deposition is approximately independent of PRF, but does depend on the size of the discharge region which can have some dependence on PRF (see [14]). A typical value of 500 $\mu J/cm^3$ will be used for comparison between model and experiment.

The two parameters that are varied to explore all configurations of strategies 1–4 (sections 4–7) are the pulse repetition frequency and the timing of the discharge relative to the flame front location at start of pulsing. The pulse repetition frequency is varied between 2, 5 and 8 kHz. 8 kHz is the highest PRF that could be used in the experiment and still obtain reliable high speed video for flame speed calculation.

A test is performed by igniting the mixture with a conventional spark plug. The high speed video and plasma are triggered some delay after this. The timing of the plasma is adjusted so that it comes on when the flame is at different positions relative to the electrode. There is some variability in the flame propagation, but it is repeatable enough that the position of the flame when the plasma was turned on was reproducible to within a couple millimeters. Tests were spaced a minimum of 30s apart to ensure adequate time for gas replenishment and cooling.

3.2. Numerical model parameters

All simulations were conducted in a constant-height channel with 3.5 mm height. The fresh reactant gas is initialized at 300K, 1atm, and with composition CH_4:O_2:N_2 = 1:2:7.52 (stoichiometric). Oncoming gas speed is initially set at 5 cm/s, but due to the non-reflecting boundary

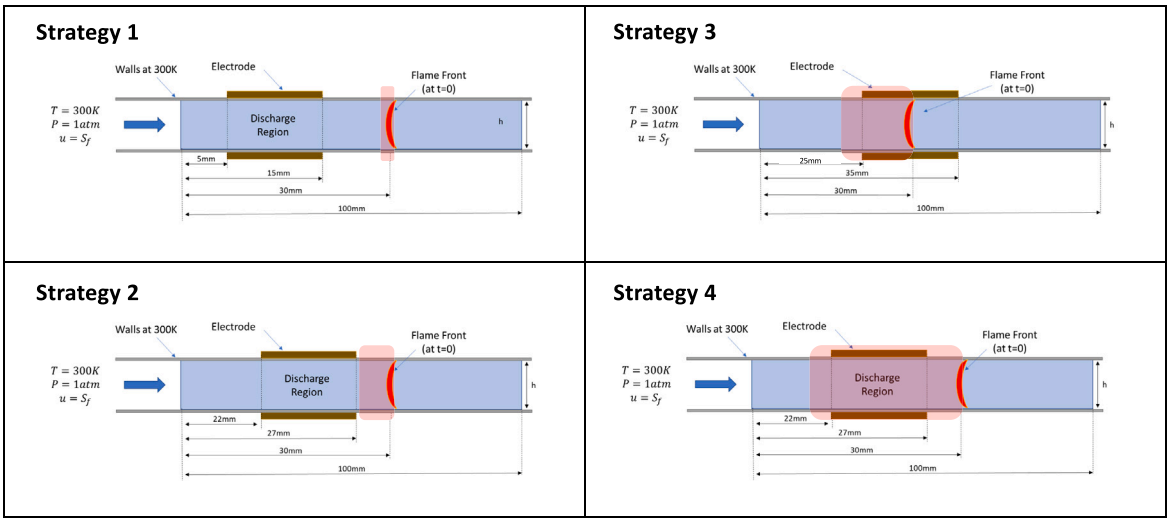

Fig. 6. Strategies of plasma–flame actuation studied in this work. The shaded red regions indicate the region of propagation of the flame during discharge pulsation in each configuration, and the dimensions correspond to the simulated parameters.

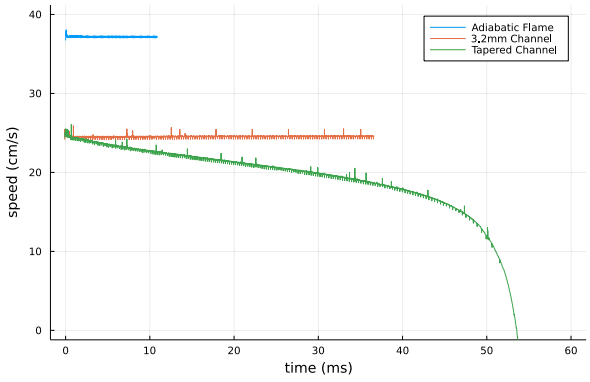

Fig. 7. Calculated flame speed for constant-height channel burner and tapered geometry from the experiments.

condition upstream of the flame, the velocity at the boundary was free to change to prevent pressure wave reflections. Once the pressure waves had subsided, the oncoming velocity would return to 5 cm/s. The GRI3.0 [28] combustion mechanism is used for all simulations and the plasma mechanism is detailed in Part I and considers detailed tracking of vibrational states and the discharge energy equation on.

The electrode size is modeled as either 5 mm or 10 mm, depending on the case. These electrodes are shorter than used in the experiments. This was done to shorten simulation times, however in the experiment the longer electrode was necessary to have a large region under it in which to view the flame for the insitu discharge configurations. These shorter electrodes also justify the choice of modeling a constant-height channel burner rather than the actual tapered geometry in the experiment, even though the model is able to handle the taper, Figs. 7 and 8 in Part I. For the shorter simulated electrode of 5 mm, the height of the channel varies less than 0.1 mm over the whole length of the electrode; and for the longer simulated electrode of 10 mm, it varies less than 0.2 mm.

In the model, flame speed measurements are made based on the motion of the flame front in time, which is effectively a lab-frame measurement. They were then converted to a laminar burning velocity using 5 cm/s as a characteristic flow rate of the unburned gas.

As in the experiment, the pulse repetition frequency was varied in each case between 2, 5 and 8 kHz. 8 kHz was taken as the baseline value and only the model output for this case is typically shown. Unless otherwise stated, the plasma discharge E/N pulse is modeled as described in Part I (Section 2.4, and Fig. 3). As described further in Part I, the E/N pulse is an input parameter based on a typical shape, rather than something solved self-consistently. Further discussion of the validity and limitations of this is discussed in Section 8.

3.3. Comparison between experiment and model

Since the model is 1D in the streamwise direction, estimates of the experimental flame speed are obtained at the centerline of the channel. Although the model and experimental parameters are selected to be comparable, the first thing to note is the higher flame speeds measured in the experiment (e.g., Fig. 4) compared to the theoretical estimates (Fig. 9, Part I), even for the baseline. The experimental lab-frame flame speed is typically between 40 and 60 cm/s at the wide end of the channel, which is higher than the expected laminar flame speed for the conditions (35–40 cm/s based on Ref. [29]). A possible explanation is due to the constrained test section and expansion of hot gases. In the model described in Part I, it was assumed that the hot gases produced by the flame can expand behind the flame front without resistance. In the experiment, there may be some resistance to this acceleration due to friction with walls or the atmospheric pressure boundary at the end of the channel. These effects may cause a pressure increase behind the flame front, which would cause an acceleration of the flame by modifying the bulk flow field. Flame curvature may also be playing an effect [29–31]. Note that the typical length of the reaction front is 1.1–1.2 times the width of the channel due to the curvature of the flame in the x–y direction. Given the absolute differences between model and experiment even for the baseline case, the comparison will be here approached in terms of percentage modification by the plasma given the corresponding baseline.

4. Strategy 1: Discharge-induced pressure waves

The first strategy considered investigates a case where the discharge is sufficiently far upstream of the flame that no kinetic or direct-heating effects can contribute to its propagation. In this case, the main mechanism of interaction is via longitudinal acoustic waves produced by the discharge. These waves allow the discharge to have a non-local effect on the flame front. It will be shown that this non-local effect is quite significant and one of the most important methods of interaction between the plasma and the flame, not always leading to a beneficial outcome. The mechanism of interaction is confirmed by the numerical simulation results.

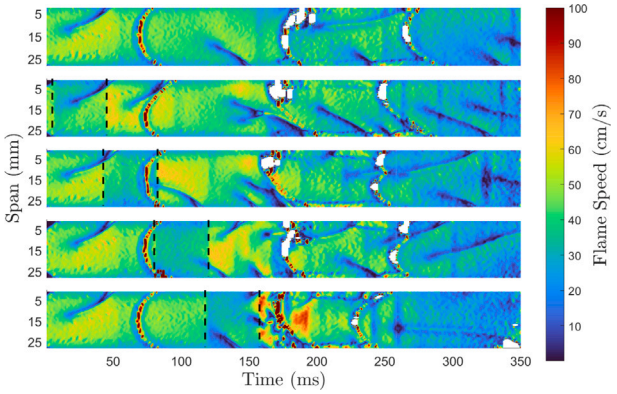

Fig. 8. Flame velocity magnitude contours, $|v_f(t,f)|$, as actuated using strategy 1. 5 tests performed with the discharge turned on at 8 kHz for 40 ms at different times. The vertical dashed black lines indicate the time the discharge is turned on/off. Top plot shows no-discharge baseline. For the second through fifth plot, the flame is approximately 80 mm, 60 mm, 40 mm and 20 mm from the electrode respectively when the discharge is first turned on.

4.1. Experimental observation of acoustic-wave induced flame speed reduction

For these experiments, the duration of the discharge was kept fixed at 320 pulses (40 ms at 8 kHz PRF) and the start time of the pulses relative to the ignition time of the flame was varied to change the position of the flame relative to the electrode at pulse onset. 5 tests were performed at each condition to demonstrate the repeatability of the outcomes. The camera frame rate was fixed at 2 kfps with an exposure time of 1/2012 s, which gave good flame resolution. Fig. 8 shows examples of the 5 conditions tested with the discharge turned on at different times, including a no-discharge baseline. Refer to Section 2.4 for how the contours should be interpreted.

For all cases shown, the flame speed noticeably decreases while the discharge is on, as evidenced by the blue-shift of the contour plot between the black lines. This can be seen both relative to the baseline case in Fig. 8 and relative to the flame speed measured before and after the discharge is applied in the same figure. There also appears to be an increase in flame speed immediately after the discharge is removed, as evidence by the red-shift of the contours relative to the baseline.

The effect of the discharge is felt by the flame within a couple milliseconds of it being turned on/off. It may even be faster than this, but the camera cannot resolve at better than 1–2 ms resolution with the current settings, so it can be said that 1 ms is an upper bound on the time it takes for the flame to be affected by the discharge. The feature visible at about 75 ms in all contours represents the flame passing under the obstruction marked as B and located at about x = 40 mm (see Section 2.3), so as a lower limit the effect of the discharge propagates at a speed of 45 mm/1 ms = 45 m/s. This is several orders of magnitude faster than the bulk flow velocity and is >10% the speed of sound. In the absence of other processes in the system capable of traveling at faster than this speed, it is concluded that the decrease in flame speed observed within 1 ms of the discharge being turned on must be caused by acoustic waves, as will be confirmed by the model (Section 4.2). Similarly, with the exception of the bottom plot in Fig. 8, there is not enough time for the radicals produced by the discharge to be transported to the flame front by diffusion or bulk fluid flow, so the flame speed increase is likely also caused by processes traveling at the sound speed.

Since the pressure waves travel only along the flow direction, it is expected that their effect should be mostly felt by the streamwise component of the velocity, with the spanwise component unaffected. This is indeed the case, as shown in Fig. 9.

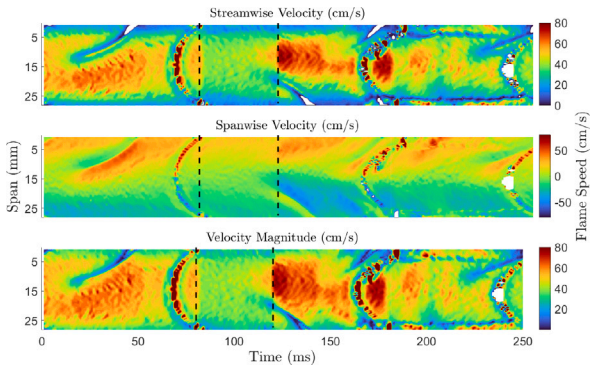

Fig. 9. Components of flame speed when discharge is applied ahead of the flame (strategy 1). 8 kHz PRF, discharge turned on for 40 ms starting when the flame is approximately 40 mm from the edge of the electrode and ending when it is approximately 20 mm away from the edge of the electrode.

4.2. Model prediction of acoustic waves

The numerical model is here used to confirm that the flame speed reduction observed in the experiment using strategy 1 is indeed due to pressure-wave disturbances and to determine the source of these perturbations.

Fig. 10 shows results of a representative simulation with the discharge applied ahead of the flame. From the graph of flame speed, the discharge causes the flame to slow down in the lab frame. The amount of decrease is approximately 5.5 cm/s, or 20% of the unperturbed flame speed. The bottom right figure shows the change in internal energy of the gas. It is approximately 540 μJ/cm^3 per pulse once the quasi-steady state has been reached. From the detailed energy balance done in Part I, this energy is approximately equal to the electrical energy input by the discharge. This energy input causes a nearly instantaneous pressure increase on the order of up to 80 Pa under the electrode. When this pressure wave is observed at a location in the unburnt gas ahead of both the electrode and flame front, its amplitude is roughly half of the initial value (bottom left figure). The reason for this halving is that the pressure wave propagates as a plane wave in two directions, with each direction getting half the energy. The pulse seen away from the electrode does have a larger width; this is due to the energy input occurring over a distributed region and diffusion terms causing wave spreading. The minor amplitude perturbations after the main energy pulse are caused by partial reflection when the wave encounters the density gradient at the flame front, discussed further below. From the bottom left graph, the pressure wave causes a peak velocity perturbation of about 7.5 cm/s as compared to the inlet flow at the start of the simulation.

The instantaneous reduction in flame speed in the lab frame (blue line in top right graph) is considerably more than the perturbation in the velocity in the unburnt flow (bottom left graph), however it is comparable to the perturbation in the velocity measured just downstream of the flame front, shown in Fig. 11, which is close to 20 cm/s.

The pressure waves were confirmed to travel at the local speed of sound of the gas, and the success of the non-reflecting boundary condition (see Part I) also demonstrates that this is the case. The amplitude is several tens of pascals. Taking a characteristic value of 30 Pa, this corresponds to a sound pressure level (SPL) of 124 dB by Eq. (9), where P_0 is the reference pressure, $P_0 = 20$ μPa.

$$\mathrm{SPL}[dB] = 20\log_{10}\left(\frac{P}{P_0}\right) \tag{9}$$

To summarize, the model predicts the formation of pressure waves as a result of the energy deposited by the discharge. These waves are caused both by the thermal energy input from the discharge (fast/slow-gas heating) and by partial oxidation of the premixed methane–air

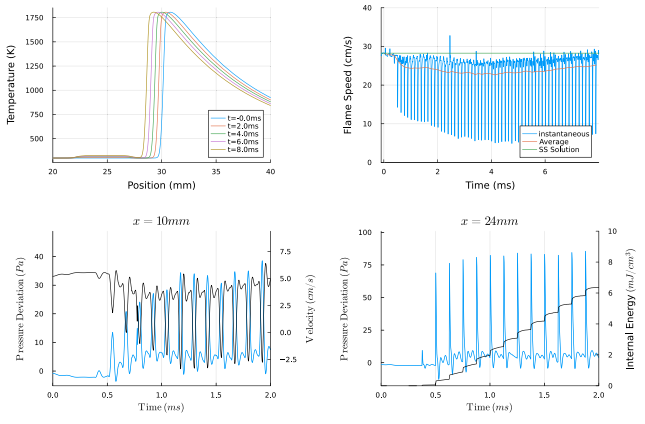

Fig. 10. Summary of simulation performed with discharge ahead of the flame (strategy 1). CW from top left: instantaneous temperature profile at several locations; measured flame speed from model; pressure (blue) and change in internal energy at a location under the electrode; pressure (blue) and local gas velocity at a location far away from the electrode in the unburnt gas. Electrode located at $x \in [22, 27]$ mm, PRF = 8 kHz.

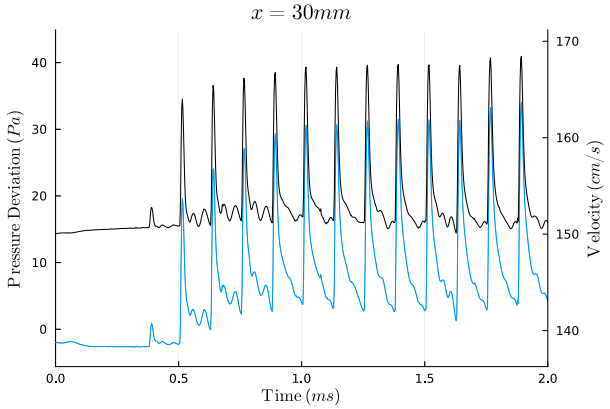

Fig. 11. Pressure (blue) perturbation and velocity 0.5 mm behind flame front. Results using strategy 1.

mixture, as was demonstrated by the existence of these pressure waves even when gas heating was not considered during the discharge (see Ref. [32]). The pressure waves locally perturb the flow velocity and are predicted to cause a flame speed decrease. Several simulations were run with a discharge energy deposition of approximately 540 μJ/cm^3 per pulse with varying levels of effect, but in all cases the flame front was slowed when the discharge was applied in the unburnt gas ahead, as was observed in the experiment.

5. Strategy 2: Discharge pre-treatment of reactants

The second strategy considered is pre-treatment of reactants by the discharge, where the discharge is applied ahead of the flame but close enough that the produced species and elevated temperatures persist until the flame reaches the electrode.

In both the experiments and the numerical model, the discharge is applied for a fixed amount of time and then turned off just before the flame reaches the electrode. The flame then propagates into a region of gas that has been pre-treated with the discharge. This configuration differs from the previous section because the flame is close enough to the electrode that discharge-created species and heating persists until the flame enters the discharge region. In the previous case, with the exception of the bottom plot in Fig. 8, the discharge was far enough

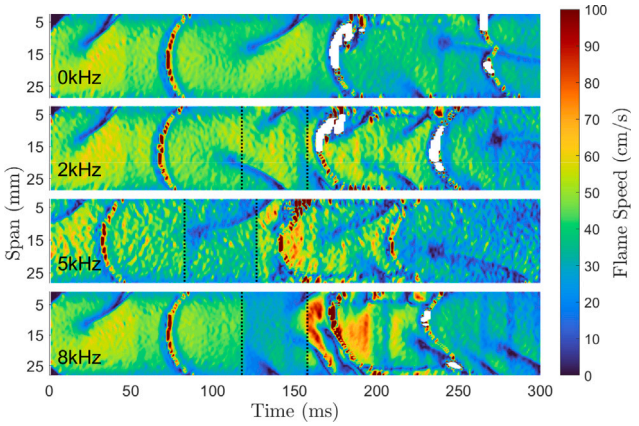

Fig. 12. Experimentally measured flame speed magnitude with discharge applied to pre-treat reactants (strategy 2). Discharge on/off marked by vertical dashed black lines. Top to bottom: 0 kHz (no discharge), 2 kHz, 5 kHz, 8 kHz. For all cases, the leading edge of the flame is approximately 20 mm ahead of the electrode when the discharge starts and 0–5 mm from the edge when it turns off.

ahead of the flame that the flame did not interact *locally* with the pre-treated gas until a long time had passed, by which point the radicals would have recombined. By turning the discharge off before the flame reaches the pre-treated region, the effect of pressure waves interfering with the flame can be removed while the flame is interacting with the pre-treated gas.

5.1. Experimental observation of discharge causing net acceleration of flame

Experiments are conducted at various frequencies, with the discharge initiated ahead of the flame and turned off before the flame reaches the electrode. The flame then propagates in the pre-treated reactants. The velocity magnitude contour plots for representative examples at each PRF are shown in Fig. 12. The unresolved feature encountered at 170 ms for 2 and 8 kHz, and at 150 ms for 5 kHz, is the flame reaching the left edge of the electrode and entering the pre-treated region of gas. Note that the 5 kHz case is more noisy than the others due to a higher raw frame rate being used on the video.

For the 5–8 kHz cases, it is evident that the flame speed increases as soon as the discharge is turned off, right before the flame enters the inter-electrode region. This is seen by the dark-red regions of the contour plot immediately to the right of the second dashed black line. For 2 kHz, there is some evidence of this speed increase, with more red regions seen under the electrode than in the 100 ms or so before the flame reaches it, but the effect is not as strong as in the higher frequency cases. The speedup is not maintained for the entire time the flame is under the electrode; it begins to decay within a few tens of ms after the discharge is turned off. As will be explained by the model, this is caused by two effects; (1) the pre-seeded radicals decaying without replenishment after the discharge is turned off, and (2) the advection of untreated gas into the inter-electrode region.

5.2. Model to explain mechanisms of interaction for discharge in reactant stream

The model is here used to explore the mechanisms that lead to flame acceleration for strategy 2 in more detail. To that end, the model was run at 8 kHz with the discharge applied on $x \in [22, 27]$ mm. After 8.5 ms (69 pulses), the discharge was turned off. At this point, the flame front had almost reached the edge of the electrode. The simulation was run until 30 ms, allowing the flame front to propagate into the gas that had

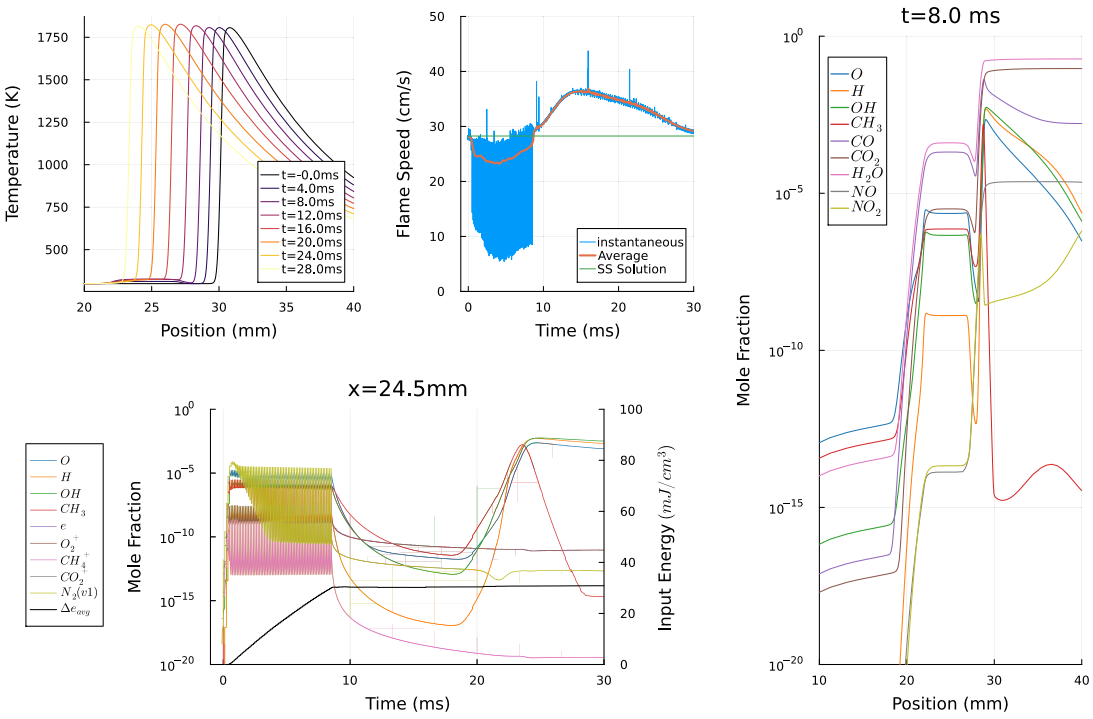

Fig. 13. Model output for 8 kHz with discharge applied ahead of flame and turned off before flame reaches electrode (strategy 2).

been pre-treated by the discharge. Results from the model are shown in Fig. 13.

Looking first at the top left plot of instantaneous temperature profiles, we see that the maximum flame temperature is slightly higher once the flame front enters the discharge region. This is a result of the pre-treated gas having an elevated temperature due to fast/slow gas heating and partial fuel oxidation. The increase in gas temperature, on the order of tens of degrees, cannot explain the flame speed increase seen in the top middle plot. The flame speed starts at 28 cm/s (in the frame of the inlet gas). There is then a decrease to around 23 cm/s due to the pressure waves produced by the discharge. The speed starts to recover as the flame approaches the electrode. As soon as the discharge is turned off, the flame speed jumps up to slightly higher than the steady state solution and then continues to increase as the flame penetrates into the discharge region. At around 14 ms, when the flame is fully under the electrode, the flame reaches its maximum speed of 37 cm/s, and then starts to decrease. The decrease can be explained by the bottom left graph, which shows the population of all the discharge-produced radicals exponentially decaying as soon as the discharge is turned off. The radical populations increase again just before 20 ms, which represents the flame passing the probe location. As the flame reaches the end of the electrode, and the radical population has decayed significantly, its speed approaches the steady-state solution. The maximum flame speed of 37 cm/s corresponds to a 9 cm/s or 32% increase over the steady-state solution. The energy input is roughly 30 mJ in 69 pulses, giving an average energy per pulse of around 540 μJ/cm^3.

The same behavior is seen at all three pulse repetition frequencies simulated, with the magnitude of the flame speed increase being proportional to the PRF as shown in Fig. 14. At 2 kHz, the flame speed increase is less than 1 cm/s (4% the steady-state solution) and at 5 kHz the flame speed increase is around 3 cm/s (13% the steady state solution). For the 5 kHz case, the energy input per pulse is roughly 325 μJ/cm^3; and, for 2 kHz, it is roughly 160 μJ/cm^3.

Compared to the experiment, for the 5 kHz case, a maximum flame speed of around 50 cm/s is observed in the inter-electrode region, corresponding to a 10 cm/s or 25% increase. For the 8 kHz case, the

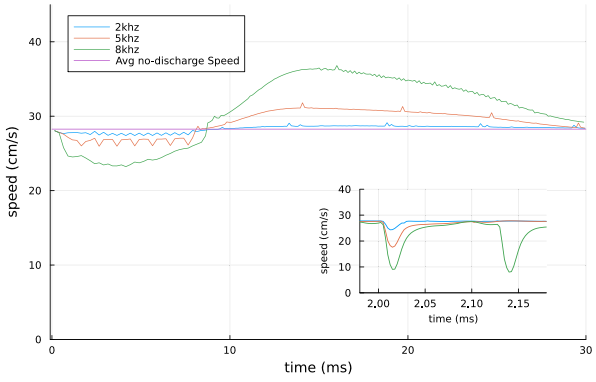

Fig. 14. Model calculated flame speed with discharge applied ahead of flame (strategy 2), at different pulse repetition frequencies. The main plot shows the average speed based on the change of flame position in 100 time steps. The inset shows the instantaneous flame speed, based on the motion between each time step.

flame speed increases to 55 cm/s while the flame is under the electrode. Comparing this to the baseline in this region of 40 cm/s gives a speed increase of 15 cm/s, corresponding to a 37% increase.

Compared to the model, the prediction at 8 kHz is closer than at 5 kHz. Experiments show that the per-pulse energy should be independent of pulse repetition frequency [14]; however the model predicts an energy that increases with pulse repetition frequency given the synergistic effect of the pulses. In this case, we are underestimating the energy input at 5 kHz and better capturing the value at 8 kHz, which explains the better agreement at 8 kHz and the underestimated flame speed increase by the model at 5 kHz.

6. Strategy 3: Insitu discharge

In this configuration, the discharge is turned on once the flame is already under the electrode, in a strategy known as insitu actuation.

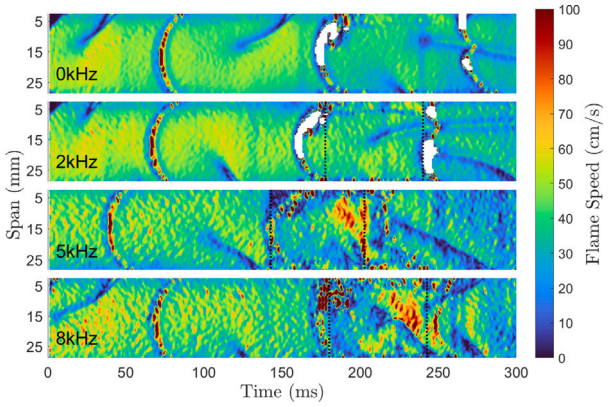

Fig. 15. Experimentally measured flame speed for insitu discharge configuration (strategy 3). Vertical dashed black lines indicate time discharge is turned on/off. Top to bottom: No discharge; discharge with PRF 2 kHz, 5 kHz, and 8 kHz.

This strategy allows for direct overlap of the plasma-created species and heat release with the flame reaction front.

6.1. Experiments with discharge applied insitu

Fig. 15 shows the flame speed contours for the case with discharge applied while the flame is underneath the electrodes, for various pulse repetition frequencies.

In all cases, when the discharge is turned on, there is an initial decrease in flame speed. This is imperceptible in the 2 kHz case, but is more noticeable at the higher PRF. After 10–20 ms have passed, the flame speed starts to noticeably increase to a value much higher than the case with no discharge, as evidenced by the dark red regions of the contour plot for the 5 and 8 kHz cases. This behavior is repeatable across tests.

Qualitatively, the disruptive effect of the discharge is experienced by the flame immediately after the electrical signal is turned on, as explained for strategy 1 (Section 4), while the beneficial effect takes time to accumulate. This delayed response can be explained by the different mechanisms. The disruptive effect is caused by a gas dynamics phenomenon (the pressure wave), while the acceleration is due to a kinetic and possibly thermal enhancement, which will take longer due to the inertia of the flame. The flame propagates by having radicals and heat diffuse ahead of it and these processes will not be instantly changed by applying the discharge. Finally, a decrease in flame speed as the flame approaches the right edge of the electrode in the 8 kHz case is observed, which will be further investigated by the numerical model.

6.2. Comparison with model for insitu strategy

The model outputs for the case of 8 kHz with the discharge applied insitu are shown in Fig. 16.

As in the experiment, the disruptive effect of the pressure waves created by the discharge, leading to a reduction in the flame speed, happens in advance of any enhancement. After a couple milliseconds, the flame speed starts to increase due to the growing pool of radicals under the electrode. The peak (average) flame speed reached in this insitu configuration is 38 cm/s, which is comparable to the discharge-ahead configuration and corresponds to a 10 cm/s, or 36%, increase in flame speed, relative to the steady state solution. As the flame reaches the edge of the electrode, there is a rapid drop in flame speed to a level slightly below the steady state solution. The rapid drop in flame speed starts just before the flame reaches the edge of the electrode; looking at the top-center plot of Fig. 16 the peak speed is reached around 13 ms,

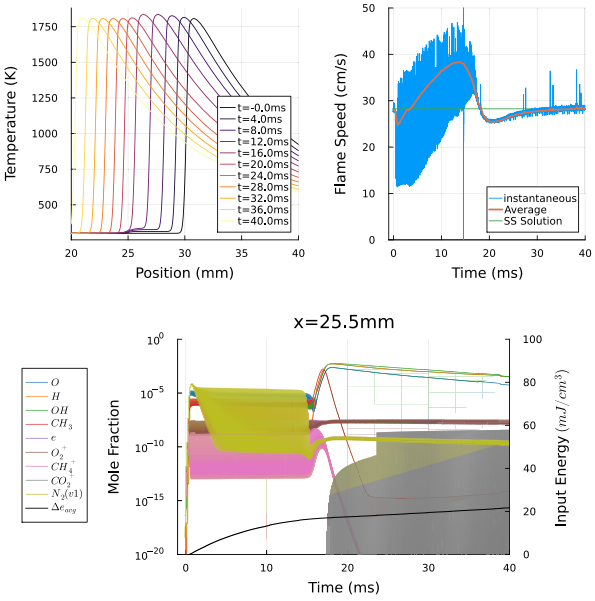

Fig. 16. Model output for 8 kHz PRF applied on $x \in [25, 35]$ mm, *insitu* configuration (strategy 3).

at which point the flame front is located around 26–27 mm (see top left plot), which is 1–2 mm from the electrode edge. The reason for this is likely that the preheat convection/diffusion zone of the flame extends for a few millimeters ahead of the flame front itself, so even though the flame front itself has not reached the edge of the electrode, this preheat zone has. The cause of the under-shoot in flame speed is not known for sure. One possible cause is that the flame was traveling too fast under the electrode, and there was not sufficient time for the heat released in the reaction zone to diffuse far enough into the oncoming gas to sustain the steady state flame speed in the absence of the discharge produced radicals. The bottom left plot of the figure illustrates that the effect of the discharge is most pronounced in the cold gases ahead of the flame. As soon as the flame front reaches the probe location, at around 14–15 ms, the pulsations are no longer visible and the curves of radical populations become smooth. This is caused by the thermal mechanism of radical production near the reaction front becoming much faster than the discharge production mechanism. The energy input past this point is also significantly reduced.

A comparison of the effects of pulse repetition frequency in the model for the insitu configuration is shown in Fig. 17. As in the experiment, the effect of the discharge is proportional to the pulse repetition frequency, with all PRF cases showing the same general trends as 8 kHz but with reduced magnitude. The net flame speed increase, as well as the undershoot at start and end of actuation, are most noticeable in this plot and are all amplified with frequency.

Finally, it is useful to compare the quantitative estimations of model and experiment. The model predicts a flame speedup of about 5 cm/s (18%) in the 5 kHz case, and 10 cm/s (36%) in the 8 kHz case. The experiments show a maximum speed of about 58 cm/s in the 5 kHz case and 60 cm/s in the 8 kHz case, a speedup of 45% and 50% respectively with respect to the corresponding baseline. These are both a bit higher than seen in the model, and might be attributed to the longer electrodes used in the experiment. This will be justified in the next section. Another point of comparison is the time it takes for the beneficial effect of the discharge to be experienced. In the model, this takes 5–10 ms, while in the experiment it is closer to 20 ms. One possible explanation for this is the uniformity of the discharge. In the experiment, the discharge always appeared in the form of micro-discharges when applied in the unburnt gas (see [13,14]). The micro-discharge structure caused non-uniform energy deposition and

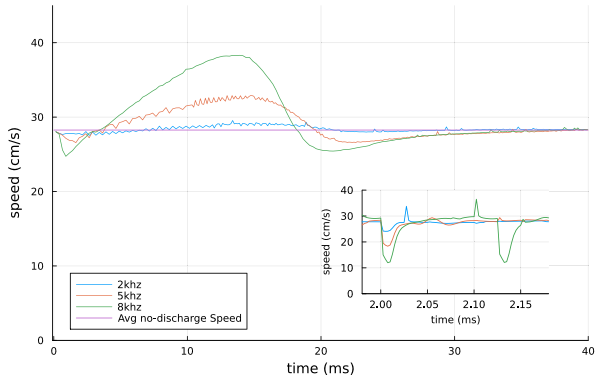

Fig. 17. Modeled flame speed for different pulse repetition frequencies and insitu discharge (strategy 3). Main graph shows average speed, based on motion in 100 timesteps. Inset shows a close-up view of instantaneous flame speed, measured based on motion every time step, immediately after a pulse.

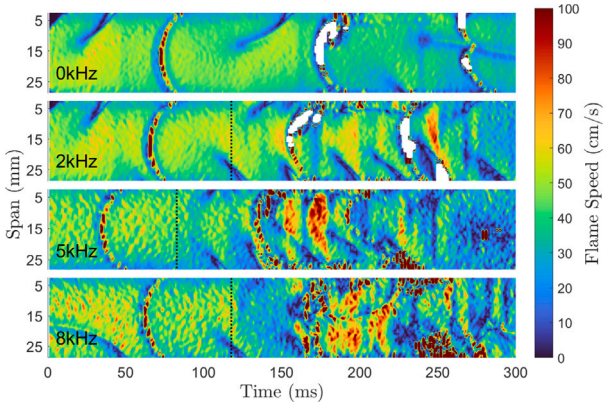

Fig. 18. Experimentally measured flame speed for ahead/insitu discharge configuration (strategy 4). Vertical dashed black lines indicate time discharge is turned on/off.

radical seeding. With this morphology, there are additional time scales; the timescale of the discharge-produced radicals to diffuse away from the micro-discharges and fill the volume, and the time it takes for the flame to reach the hot-spots created by the micro-discharges. This non-uniformity of the discharge may be responsible for the delayed impact of the plasma on the flame.

7. Strategy 4: Combined pre-treatment and insitu discharge

The final configuration tested is the combined strategy reactant pre-treatment + *insitu* discharge. In this case, the discharge is turned on while the flame is still ahead of the electrode. The flame then penetrates the inter-electrode region while the pulses are still being applied.

7.1. Experiments combining discharge applied ahead and insitu

Fig. 18 shows the contour plots for experimentally measured flame speed when combining the pre-treatment and insitu strategies. A representative case for each pulse repetition frequency is shown.

For PRF 5 kHz and 8 kHz, the flame speed decreases as soon as the discharge is turned on, and then increases significantly while the flame is under the electrode. There is some evidence of a flame speed decrease when the flame reaches the right edge of the electrode (around 200 ms for 5 kHz and 230 ms for 8 kHz), which will be investigated with the model. For 2 kHz, the effect of the discharge is hard to distinguish in the experiment, given the noise introduced by having to use the higher frame rate videos and taking numerical derivatives.

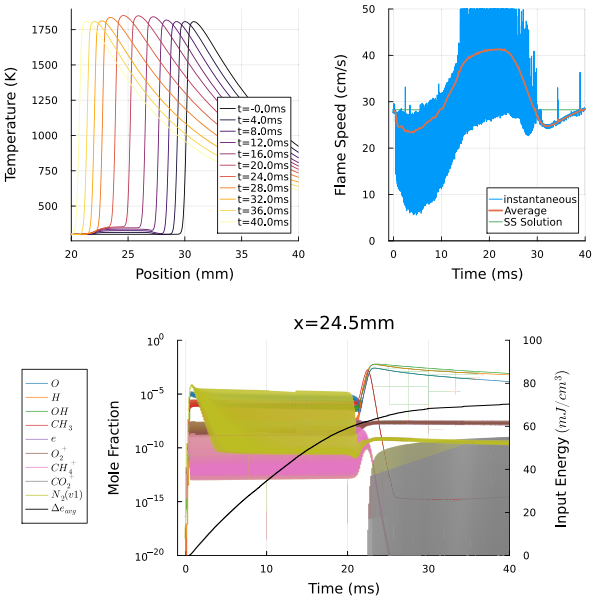

Fig. 19. Model output for 8 kHZ PRF applied on $x \in [22, 27]$ mm, *ahead/insitu* configuration (strategy 4).

7.2. Comparison with model for combined ahead+insitu strategy

The model outputs for the case of 8 kHz with the discharge applied both ahead and insitu is shown in Fig. 19. In this case, the initial disruption to flame speed (top-center plot) lasts for longer than in the insitu only strategy (strategy 3, Section 6) because the beneficial effects of the discharge are not felt until the flame starts to approach the electrode. The flame starts to accelerate around 6 ms, which is before the flame front reaches the electrode but around the time that the edge of the convection–diffusion zone encounters the discharge produced radicals. The peak flame speed is attained at 22 ms, when the flame is located around x = 24 mm. As with the insitu configuration, this is about 2 mm before the flame reaches the electrode edge. The peak flame speed attained is 42 cm/s, 14 cm/s (50%) higher than the steady state solution. This is a more significant increase than was seen in the insitu case (strategy 3). The reason for the greater effect is twofold. The discharge has been on for longer, so there is a greater temperature increase in the unburnt gas, up to 100K based on the top left plot. Also, the flame sees the discharge effect for longer than in the insitu case. The effect begins to be felt before the flame even reaches the electrode, and when the flame does reach the electrode the radical populations have already achieved their quasi-steady state. In the insitu case, Fig. 16, the flame looks to still be accelerating just before it reaches the point where the edge of the electrode causes the flame to slow down, while in Fig. 19, the acceleration seems to be slowing, suggesting the flame speed is plateauing. The undershoot in flame speed after the flame leaves the electrode region is also seen in this case.

As before, a comparison of the effects of pulse repetition frequency in the model for the combined strategy is shown in Fig. 20. As seen previously, the effect of the discharge is proportional to the pulse repetition frequency, with all PRF cases showing the same general trends as 8 kHz but with reduced magnitude.

In terms of quantitative comparison with the experiment, from Fig. 20, the model predicts a 25% speedup in the 5 kHz case and a 50% speedup in the 8 kHz case. In the experiment, at 5 kHz the flame speed reaches a maximum of around 65 cm/s in each of the tests and the average speed under the electrode is around 55 cm/s, a 37% speedup. For 8 kHz, the maximum is around 75 cm/s with a typical value of around 60 cm/s, a 50% speedup. Comparing both, the model

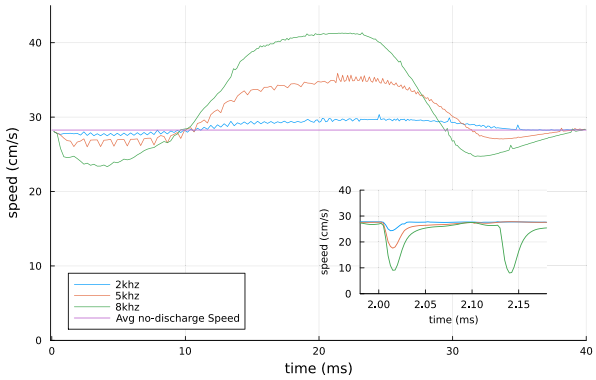

Fig. 20. Modeled flame speed for different pulse repetition frequencies and coupled ahead/ insitu discharge (strategy 4). Main graph shows average speed, based on motion in 100 timesteps. Inset shows a close-up view of instantaneous flame speed, measured based on motion every time step, immediately after a pulse.

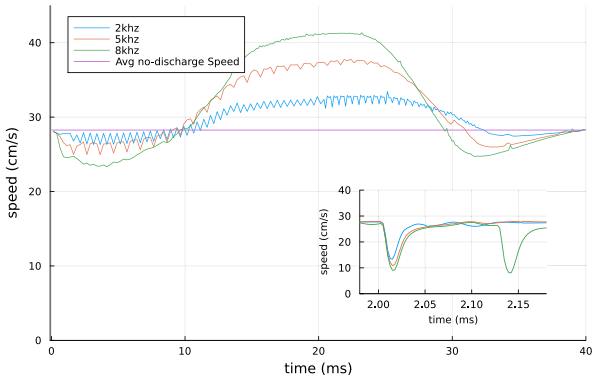

Fig. 21. Comparison of flame speed for models with discharge ahead/insitu (strategy 4) with energy scaled to have approximately PRF-independent per pulse energy deposition, and comparable to the experimental value. Compare to Fig. 20.

Table 1
Summary table for different plasma actuation strategies, comparing flame speed modification estimated by model and experiment. ↓ indicates flame speed decrease. ↑ indicates flame speed increase.

Strategy	Experiment	Model	Notes
1	↓ 30–40%	↓ 30%	Pressure waves disrupt flame
2	↑ 37%	↑ 30%	Enhancement decreases with time after discharge stops
3	↑ 50%	↑ 35%	Model enhancement limited by electrode size
4	↑ 50%	↑ 50%	Plateau in flame speed reached

for 8 kHz predicts a reasonable relative flame speed increase under plasma influence, while the 5 kHz case under-predicts. Looking at energy, at 8 kHz the model estimated an average per-pulse energy of 500 $\mu J/cm^3$. Accounting for electrode size, this is roughly equal to the energy input from the experiment. As in the previous case, for the 5 kHz case, the model underpredicts the energy input and so the flame speed enhancement.

8. Discussion

Model and experiment were used to systematically evaluate the influence of plasma location, relative to the flame front, on the flame speed. The qualitative observations, including flame speed acceleration, and undershoots at start and end of actuation, were well reproduced by both model and experiment. A sustained beneficial effect of plasma, quantified as up to a 50% flame speed increase at the highest pulse repetition frequency (8 kHz) tested was predicted, attributed to a combined thermal-kinetic effect. Adverse effects of the plasma were also observed, quantified as a net flame speed decrease of 30%, and attributed to pressure disturbances. A summary table of the different strategies, as calculated by the model and observed in the experiment is given in Table 1.

The quantitative agreement between model and experiment, in terms of percentage increase or decrease in the flame speed compared to the corresponding no-plasma baseline, was much better for the 8 kHz case than the 5 kHz and was attributed to the better agreement in the volumetric energy input between both.

One of the limitations of the numerical model is that the profile of the reduced electric field (E/N) is an input to the model, and this fixes the energy delivery to the gas and ignores the two-way coupling between plasma and flame [13,14]. The E/N temporal and spatial evolution is difficult to measure in experiments, although recent advances in the E-FISH method have allowed it to be probed directly [33]. Modeling the DBD itself is another option for generating reasonable profiles of E/N [34,35]. For the results presented in this work, the same E/N profile as proposed in [34] was used. As a result, the energy input per pulse in the model is fixed by this choice and changed with the pulse repetition frequency, while in the experiments such a dependency was not observed (the per-pulse energy was constant with frequency) [14]. The explanation for this is the self-limiting property of DBD discharges. As soon as the electron number density reaches a sufficient level, space charge shielding reduces the applied field and further ionization is prevented. However, the model does not self-consistently solve for this shielding effect and determines energy input purely based on the user-set reduced electric field, which is kept constant across simulations.

To test this hypothesis, and since the 8 kHz case deposited approximately the right amount of energy compared to the experiments, the 2 and 5 kHz cases are here modified to match that same energy. To that end, the profile of E/N is scaled to achieve the same maximum electron number density during pulse application regardless of PRF, with the justification that this critical number density represents the point at which space-charge shielding causes the field to decrease. Details of the method to scale the E/N waveform to deliver a PRF-independent per-pulse energy are provided in the supplementary material accompanying this paper.

The results for the same case as presented in strategy 4 (Section 7: ahead+insitu discharge), but with the E/N profile modified to deliver roughly 500 $\mu J/cm^3$ per pulse independent of the PRF, are shown in Fig. 21. This figure should be compared to Fig. 20 which has the same energy delivery for the 8 kHz case and lower energy deliveries for the 2 and 5 kHz cases respectively.

As a result of the increased energy deposition, the impact on the flame speed is also increased. Previously, the 2 kHz PRF case with this electrode configuration had a maximum flame speed increase of 2 cm/s (see Fig. 20), now it is approximately 5 cm/s or 18%. For the 5 kHz case, a maximum flame speed of 37 cm/s is now obtained, which corresponds to a 9 cm/s or 32% increase above the baseline, which is closer to the enhancement observed in the experiment of 37% increase.

9. Conclusion

This work has systematically explored the impact of nanosecond repetitively pulsed (NRP) discharges on laminar flame speed for premixed methane–air, emphasizing how the relative positioning of the discharge and the flame front determines whether plasma acts to accelerate or disrupt the flame. When the flame and discharge are separated in space, acoustic perturbations generated by the discharge induce a noticeable reduction in flame speed. Closer placement of the discharge,

relative to the flame front, leads to pre-treatment of the incoming reactants, so that the flame encounters elevated temperatures and a radical pool that cause a substantial speedup once any disruptive pressure waves subside. Direct overlap between discharge and flame front (the insitu strategy) yields a net acceleration, driven by plasma-supplied heat and reactive species. Combining the pre-treatment and insitu modes produces the most pronounced and sustained enhancements, since the flame is preconditioned and then continuously sustained by the plasma as it passes under the electrode. All the effects are accentuated by increasing the pulse repetition frequency.

From a quantitative perspective, the maximum flame speed enhancement achieved for this stoichiometric methane–air mixture was about 50% for both model and experiment, and corresponded to the combined pre-treatment+insitu strategy. In this case, the flame speed was sustained for over 10 ms indicating the maximum benefit at those conditions had been achieved and was not limited by the electrode length. This was however limited by the 8 kHz frequency selection, and will likely increase by using higher values of this electrical parameter.

Both experiments and the one-dimensional plasma–combustion model presented in Part I agree on these flame-speed modifications and the model is used to capture the underlying mechanisms: pressure-wave disruption, partial oxidation upstream of the flame, and thermal-chemical enhancement near the reaction front. While the model reproduces the main qualitative trends, quantitative comparisons show that deviations in per-pulse energy deposition and two-dimensional flow effects can influence the timing and magnitude of plasma-driven flame acceleration. A main limitation of the model was the prescribed E/N temporal waveform, as it predefined the energy input which did not match the experimental values at the lower frequencies tested. Correcting for this energy delivery allowed to achieve a much better agreement between model and experiment.

Overall, these findings demonstrate that carefully targeted NRP discharges can both promote and hinder flame propagation, depending on how the flame and plasma are arranged in space and time. By employing a controlled narrow-channel burner as both a numerical and experimental platform, this study systematically varied discharge placement and pulse repetition frequency, yielding clear guidelines for optimal actuation strategies. Moreover, by comparing different configurations within a unified framework, the results capture the envelope of plasma actuation performance on a fundamental combustion metric (laminar flame speed) and clarify how disparate outcomes often arise from differences in discharge-flame positioning, timing, and energy delivery.

CRediT authorship contribution statement

Colin A. Pavan: Writing – original draft, Visualization, Software, Methodology, Investigation, Formal analysis, Data curation, Validation. **Carmen Guerra-Garcia:** Writing – review & editing, Writing – original draft, Supervision, Resources, Project administration, Methodology, Funding acquisition, Conceptualization.

Declaration of competing interest

The authors declare that they have no known competing financial interests or personal relationships that could have appeared to influence the work reported in this paper.

Acknowledgments

This work has been supported by the Office of Naval Research (ONR), USA Award Number N00014-21-1-2571, and by the National Science Foundation (NSF), USA Award Number 2339518. C.P. was partially supported by a Mathworks Fellowship at the time the work was performed.

Appendix A. Supplementary data

Supplementary material related to this article can be found online at https://doi.org/10.1016/j.combustflame.2025.114475.

References

[1] N.L. Aleksandrov, S.V. Kindysheva, I.N. Kosarev, S.M. Starikovskaia, A.Y. Starikovskii, Mechanism of ignition by non-equilibrium plasma, Proc. Combust. Inst. 32 I (1) (2009) 205–212.
[2] I.N. Kosarev, N.L. Aleksandrov, S.V. Kindysheva, S.M. Starikovskaia, A.Y. Starikovskii, Kinetics of ignition of saturated hydrocarbons by nonequilibrium plasma: CH4-containing mixtures, Combust. Flame 154 (3) (2008) 569–586.
[3] I.N. Kosarev, N.L. Aleksandrov, S.V. Kindysheva, S.M. Starikovskaia, A.Y. Starikovskii, Kinetics of ignition of saturated hydrocarbons by nonequilibrium plasma: C2H6- to C5H12-containing mixtures, Combust. Flame 156 (1) (2009) 221–233.
[4] W. Kim, M. Godfrey Mungal, M.A. Cappelli, The role of in situ reforming in plasma enhanced ultra lean premixed methane/air flames, Combust. Flame 157 (2) (2010) 374–383.
[5] M.S. Bak, H. Do, M.G. Mungal, M.A. Cappelli, Plasma-assisted stabilization of laminar premixed methane/air flames around the lean flammability limit, Combust. Flame 159 (10) (2012) 3128–3137.
[6] S. Barbosa, G. Pilla, D.A. Lacoste, P. Scouflaire, S. Ducruix, C.O. Laux, D. Veynante, Influence of nanosecond repetitively pulsed discharges on the stability of a swirled propane/air burner representative of an aeronautical combustor, Philos. Trans. R. Soc. Lond. Ser. A Math. Phys. Eng. Sci. 373 (2048) (2015) 20140335.
[7] G. Vignat, N. Minesi, P.R. Soundararajan, D. Durox, A. Renaud, V. Blanchard, C.O. Laux, S. Candel, Improvement of lean blow out performance of spray and premixed swirled flames using nanosecond repetitively pulsed discharges, Proc. Combust. Inst. 38 (4) (2021) 6559–6566.
[8] M. Castela, B. Fiorina, A. Coussement, O. Gicquel, N. Darabiha, C.O. Laux, Modelling the impact of non-equilibrium discharges on reactive mixtures for simulations of plasma-assisted ignition in turbulent flows, Combust. Flame 166 (2016) 133–147.
[9] L. Massa, J.B. Freund, Plasma-combustion coupling in a dielectric-barrier discharge actuated fuel jet, Combust. Flame 184 (2017) 208–232.
[10] M.D. Evans, J.M. Bergthorson, S. Coulombe, Actuation of a lean-premixed flame by diffuse non-equilibrium nanosecond-pulsed plasma at atmospheric pressure, J. Appl. Phys. 122 (17) (2017).
[11] A. Elkholy, Y. Shoshyn, S. Nijdam, J.A. van Oijen, E.M. van Veldhuizen, U. Ebert, L.P. de Goey, Burning velocity measurement of lean methane-air flames in a new nanosecond DBD microplasma burner platform, Exp. Therm. Fluid Sci. 95 (January) (2018) 18–26.
[12] T. Ombrello, S.H. Won, Y. Ju, S. Williams, Flame propagation enhancement by plasma excitation of oxygen. Part II: Effects of O2(a1Δg), Combust. Flame 157 (10) (2010) 1916–1928.
[13] C. Guerra-Garcia, C.A. Pavan, The backward problem in plasma-assisted combustion: Experiments of nanosecond pulsed discharges driven by flames, Appl. Energy Combust. Sci. 15 (March) (2023) 100155.
[14] C.A. Pavan, C. Guerra-Garcia, Nanosecond pulsed discharge dynamics during passage of a transient laminar flame, Plasma Sources Sci. Technol. 31 (11) (2022) 115016.
[15] C.A. Pavan, C. Guerra-Garcia, Two-way coupling of flame and nanosecond pulsed dielectric barrier discharge in a mesoscale burner, AIAA SciTech Forum Expo. 2024 (January) (2024) 1–7.
[16] J. George, C. Menon, Electrical and optical properties of electron beam evaporated ITO thin films, Surf. Coat. Technol. 132 (1) (2000) 45–48.
[17] C.A. Pavan, S.R. Rao, C. Guerra-Garcia, Tutorial: electrical measurements in nanosecond pulsed plasma reactors, J. Phys. D Appl. Phys. 58 (2025) 032502.
[18] C. Clanet, G. Searby, On the "tulip flame" phenomenon, Combust. Flame 105 (1–2) (1996) 225–238.
[19] M. Gonzalez, R. Borghi, A. Saouab, Interaction of a flame front with its self-generated flow in an enclosure: The "tulip flame" phenomenon, Combust. Flame 88 (2) (1992) 201–220.
[20] B. Ponizy, A. Claverie, B. Veyssière, Tulip flame - the mechanism of flame front inversion, Combust. Flame 161 (12) (2014) 3051–3062.
[21] D. Sharp, An overview of Rayleigh-Taylor instability, Phys. D 12 (1–3) (1984) 3–18.
[22] S. Nagaraja, T. Li, J.A. Sutton, I.V. Adamovich, V. Yang, Nanosecond plasma enhanced H2/O2/N2 premixed flat flames, Proc. Combust. Inst. 35 (3) (2015) 3471–3478.
[23] C. Guerra-Garcia, M. Martinez-Sanchez, R.B. Miles, A. Starikovskiy, Localized pulsed nanosecond discharges in a counterflow nonpremixed flame environment, Plasma Sources Sci. Technol. 24 (5) (2015) 055010.
[24] D.A. Xu, D.A. Lacoste, D.L. Rusterholtz, P.-Q. Elias, G.D. Stancu, C.O. Laux, Experimental study of the hydrodynamic expansion following a nanosecond repetitively pulsed discharge in air, Appl. Phys. Lett. 99 (12) (2011) 121502.

[25] F. Tholin, A. Bourdon, Simulation of the hydrodynamic expansion following a nanosecond pulsed spark discharge in air at atmospheric pressure, J. Phys. D Appl. Phys. 46 (36) (2013).
[26] S.B. Leonov, V. Petrishchev, I.V. Adamovich, Dynamics of energy coupling and thermalization in barrier discharges over dielectric and weakly conducting surfaces on μ s to ms time scales, J. Phys. D Appl. Phys. 47 (46) (2014).
[27] A.Y. Starikovskii, A.A. Nikipelov, M.M. Nudnova, D.V. Roupassov, SDBD plasma actuator with nanosecond pulse-periodic discharge, Plasma Sources Sci. Technol. 18 (3) (2009).
[28] G.P. Smith, D.M. Golden, M. Frenklach, N.W. Moriarty, B. Eiteneer, M. Goldenberg, C.T. Bowman, R.K. Hanson, S. Song, J.W.C. Gardiner, V.V. Lissianski, Z. Qin, GRI-Mech 3.0, URL http://combustion.berkeley.edu/gri-mech/version30/text30.html.
[29] S.R. Turns, An Introduction to Combustion: Concepts and Applications, third ed., McGraw-Hill, New York, NY, 2012.
[30] D. Veynante, L. Vervisch, Turbulent combustion modeling, Prog. Energy Combust. 28 (3) (2002) 193–266.
[31] T.C. Lieuwen, Unsteady Combustor Physics, first ed., Cambridge University Press, New York, NY, 2012.
[32] C.A. Pavan, C. Guerra-Garcia, Modeling flame speed modification by nanosecond pulsed discharges to inform experimental design, in: AIAA SCITECH 2023 Forum, no. January, American Institute of Aeronautics and Astronautics, Reston, Virginia, 2023, pp. 1–15.
[33] A.C. Rousso, B.M. Goldberg, T.Y. Chen, S. Wu, A. Dogariu, R.B. Miles, E. Kolemen, Y. Ju, Time and space resolved diagnostics for plasma thermal-chemical instability of fuel oxidation in nanosecond plasma discharges, Plasma Sources Sci. Technol. 29 (10) (2020).
[34] S. Nagaraja, V. Yang, Z. Yin, I. Adamovich, Ignition of hydrogen-air mixtures using pulsed nanosecond dielectric barrier plasma discharges in plane-to-plane geometry, Combust. Flame 161 (4) (2014) 1026–1037.
[35] I.V. Adamovich, M. Nishihara, I. Choi, M. Uddi, W.R. Lempert, Energy coupling to the plasma in repetitive nanosecond pulse discharges, Phys. Plasmas 16 (11) (2009) 113505.